TECHNICAL ARTICLE

Microstructural and Mechanical Properties of Al$_2$O$_3$ and Al$_2$O$_3$/TiB$_2$ Ceramics Consolidated by Plasma Pressure Compaction

F. Rubino, G. Rotella, M. Perrella, P. Carlone [ID], and T.S. Sudarshan

Alumina oxide ceramics were produced by plasma pressure compaction (P^{2}C) sintering process. Two types of pure α-alumina (Al$_2$O$_3$) and a mixture of alumina and titanium diboride (TiB$_2$) powders were used as starting materials. Microstructure and mechanical properties, namely hardness, elastic modulus, and fracture toughness, were analyzed and correlated to the type of the sintered powders and the adopted manufacturing route. The microstructural development and the chemical composition variation induced by the sintering process were assessed by using scanning electron microscopy and x-ray diffraction. Nano-indentation and Chevron notch beam techniques were adopted to estimate the mechanical properties of the sintered ceramics. The conducted analyses show the capability of P^{2}C technique to produce sound alumina ceramics. Pure alumina bulks exhibit a good level of compaction and mechanical properties close to those achievable with conventional sintering processes, such as hot isostatic pressing or spark plasma sintering. No significant alterations in the chemical composition of the ceramics were observed. The addition of the titanium diboride in the alumina powders caused a moderate increase in the grain size lowering the hardness and Young's modulus of the sintered alumina and, at the same time, increased its fracture toughness to the occurrence of toughening mechanisms, like crack bridging and crack deflection.

1. Introduction

Alumina ceramics are widely employed in a very large number of engineering applications, ranging from ball mills, dyes, corrosion-resistant containers, and biomedical implants (Ref 1). The high melting temperature, hardness, chemical inertness, and electrical insulating properties of alumina, indeed, make this material very attractive for thermal and electrical insulation, chemical processing, bioengineering, and optics (Ref 2-5). Alumina ceramics are produced by using two approaches: liquid phase sintering (LPS), where a viscous flow is used to aid the consolidation of the alumina, and solid-state sintering. Solid-state processes are generally preferred to fabricate ceramics for high-end applications, which required elevate mechanical properties and high thermal stability, since they can produce pure bulk, having a percentage of alumina above 99.7 wt.%, with a high densification level. LPS processing can produce densities of 96 wt.% or lower, through to the use of liquid additives that form a low soluble oxide, like CaO, SiO$_2$, or MgO (Ref 6).

Slip casting and dry pressing are the most used commercial sintering techniques to fabricate alumina-based ceramics. Among these two, the latter technique allows producing high-quality alumina ceramics balancing the quality of the products and the production cost (Ref 6). Pressure-assisted sintering (hot pressing or hot isostatic pressing) accelerates the densification kinetics by exerting augmented mechanical stress at the particle boundaries and favors their packing. It allows the manufacturers to reduce the holding time and the processing temperature with respect to the pressure-less techniques, so that excessive grain growth is prevented, and lower residual porosity is achieved. Those two factors contribute to the high strength of the hot-pressed ceramics (Ref 6).

Hot-pressing techniques usually involve demanding processing conditions, characterized by high temperature (around 1600 °C) (Ref 1, 7-9), high pressure, and long holding times, ranging from minutes to hours, to obtain densification.

In ceramic manufacturing by sintering process, the densification and the coarsening mechanisms, which are responsible for grain growth, are competitive factors. While the former requires high temperature and pressure, and a long time to achieve optimal levels, these conditions promote the latter phenomenon, which is detrimental to the mechanical and electrical properties of the sintered ceramic.

Processing conditions, especially temperature and dwell time, and composition have a strong influence on the final microstructure of the sintered products, causing changes in the

F. Rubino, Department of Chemical, Energetic and Mechanical Technology, Escuela Superior de Ciencias Experimentales y Tecnología, King Juan Carlos University, Mostoles (Madrid), Spain; G. Rotella, Department of Engineering for Innovation, University of Salento, Lecce, LE, Italy; M. Perrella, Department of Chemical, Materials and Production Engineering, University of Napoli Federico II, Naples, Italy; P. Carlone, Department of Industrial Engineering, University of Salerno, Fisciano, SA, Italy; and T.S. Sudarshan, Materials Modification Inc., Fairfax, VA. Contact e-mail: pcarlone@unisa.it.

phase distribution and size, shape and dimensions of pores, grade of crystallinity of sintered alumina, which in turn influence the strength, the elastic moduli and creep resistance (Ref 10). Therefore, strategies and techniques that can balance these two phenomena are under study. Researchers have investigated the spark plasma sintering (SPS) process to produce compacted bulk from commercial alumina powders. The process applies a pulsed direct current to the powders during the compaction and exploits the heat source from Joule's effect to aid the densification of the sintered part minimizing the operating temperature, the applied pressure, and the holding time (Ref 11-14). This prevents the grain growth, maximizing hence the mechanical properties (hardness, flexural toughness, elastic modulus, etc.) of the sintered alumina. Studies on the sintering of α- and γ- Al_2O_3 particles by using the SPS technique reported the production of undoped and doped alumina specimens having a relative density above 99% adopting process conditions below those required by conventional processes (Ref 15-17).

In the present study, alumina samples were produced by using the plasma pressure compaction ($P^2C^©$) technique. P^2C is a plasma-assisted sintering technique allowing densification of compacted powders in a shorter time, usually dwell time ranges between 2 and 30 min depending on the initial size of powders instead of hours, and at a lower temperature than conventional sintering processes (Ref 18-24). Description of the equipment and operating principles has been omitted here for sake of brevity and can be found elsewhere (Ref 18-25).

A second strategy to control the final morphology and microstructure of the sintered ceramics to achieve good mechanical properties involves the use of additives. The addition of a micrometer or nanometer second phase within the alumina matrix has a dual effect. This approach promotes grain refinement, limiting the grain size, and preventing the grains to grow anisotropically. The use of secondary particles determines the activation of toughening mechanisms, such as crack deflection or crack bridging, which are beneficial for the fracture resistance of the ceramic. Therefore, doped alumina ceramics achieve outstanding mechanical, physical, and morphological characteristics (Ref 26, 27). Among the several additives experimented, titanium diboride (TiB_2) has been used in armor, cutting tools and wear-resistant coatings, and as a reinforcing phase within ceramic-based composite materials (Ref 28). Alumina-based Al_2O_3/TiB_2 composites have been widely explored in the last decade and found potential use as individual protective equipment, spacecraft shielding, braking system in automobiles and airplanes (Ref 27, 29)). The addition of the titanium diboride phase allows for modification of the final microstructure of the alumina matrix phase obtaining different morphologies and, in turn, tuning the mechanical and thermal performance of the composite (Ref 29). The main issue in fabricating alumina/titanium diboride composite derive from the poor sinterability, especially when higher percentages of the second phase are adopted (above 20 wt.%), which limits the densification of the powders (Ref 27). Among the manufacturing techniques investigated, such as combustion or chemical synthesis and hybridization, (Ref 30-33), hot-pressing sintering of TiB_2 and Al_2O_3 powders appeared to be a promising alternative to fabricate the alumina-based composite with a wide range of the amount of the reinforcing second phase (Ref 26, 27). The results obtained are indicative of the behavior of the composite but not conclusive, being the measured parameters strongly dependent on the morphology and the amount of the raw powders, the mixing procedure, and the sintering processes and conditions. In the present paper, the fabrication of Al_2O_3/ TiB_2 composite by plasma pressure compaction technique was investigated and the results are compared with pure alumina ceramics produced using the same sintering process. Composition, microstructure morphology, and mechanical properties have been evaluated.

2. Materials and Methods

The alumina powders were provided by CoorsTek (Golden, Colorado, USA). Three test cases have been considered, adopting different selections of the alumina powders: (a) 100% pure Al_2O_3 Grade K790; (b) 100% pure micron Al_2O_3 (sample code M100), (c) 95% Grade K790 Al203 + 5% titanium diboride (sample code K95T15). P^2C process was adopted to manufacture the bulk alumina ceramic. The micrometer alumina powders were consolidated by applying a compaction pressure of 20 MPa at a processing temperature of 1250 °C with a heating rate of 100 °C/min. The powders were poured into a graphite die and then compacted using graphite plungers. Sintering was conducted in vacuum conditions to avoid any interaction of the powders with the environment. No sintering aids or other additives, except for the titanium diboride used on purpose, were employed. During the compaction, a direct current was applied simultaneously to the external pressure of 20 MPa (Ref 24, 34). The consolidation time was ten minutes and prevents grain growth.

Specimens from each sample were cut and prepared for metallographic analysis. Samples were cut, embedded on a black Bakelite mounting resin with carbon filler, and mechanically polished up to 0.5 μm grade. Scanning electron microscopy (SEM) was used to analyze the microstructure of the sintered alumina. The average grain size of sintered alumina samples was calculated by using the line intercept method on the scanning electron microscope images of polished and etched surfaces of the specimens. ImageJ suite was used for the analysis of the microstructure. X-ray diffraction technique was used to identify the matrix and the other second phases within the microstructure. Diffractometry was performed using the conventional symmetrical Bragg Brentano configuration ($\theta/2\theta$) on a Rigaku MiniFlex 600 x-ray diffractometer (Rigaku Corporation, Tokyo, Japan) with CuKa, radiation generated at 20 mA and 40 kV. PDF-4 + 2021 database was used to analyze the patterns obtained from the diffraction tests and identify the species present in the specimens.

Nano-indentation tests were conducted on the polished specimens by using an instrumented nanoindenter (CSM). The surface of the specimens before the indentation was polished up to 0.5 μm as explained above. The machine was calibrated using a standard material (fused silica) to guarantee the accuracy of the measurements. A triangular pyramidal diamond Berkovich tip was used, with an apex angle θ of 70.3°. Figure 1 shows the applied load function with the time for the three peak loads considered, namely 100, 200, and 400 mN. The indenter was loaded at a constant rate up to the specific peak load, and after a dwell time of 10 s, it was unloaded at the same rate. The tests were set to have the same time loading of approximately 67 s. Therefore, different loading rates were adopted, equal to 200, 400, and 800 mN/min, respectively. The same dwell time of 5 s for all tests was chosen. Load and displacement were

continuously recorded along with the duration of each test, and the data collected were processed to evaluate the hardness and Young's modulus of the specimens (Ref 35). Five indentations were made for each sample.

The chevron notch beam (CNB) test was conducted according to the ASTM C 1421 standard to evaluate the fracture toughness (Ref 36). In this paper, the CNB tests were performed in three-point bending configuration (Fig. 2) under displacement control at the rate of 0.2 mm/min using MTS Insight 30 testing machine. All the experiments were conducted at room temperature (22 °C). The sample dimensions are reported in Fig. 2.

The fracture toughness K_{Ivb} is given by:

$$K_{Ivb} = Y^*_{min} \cdot \left[\frac{P_{max} \cdot S_0 \cdot 10^{-6}}{B \cdot \sqrt{W^3}} \right] \qquad \text{(Eq 1)}$$

where Y^*_{min} is the stress intensity factor coefficient as defined in the ASTM C 1421 standard, P_{max} is the maximum test load, S_0 is the support span, B is the width of the specimen and W is the thickness of the sample.

The dimensions of small specimens made difficult to use traditional transducers, such as extensometers, for the measurement of crack mouth opening displacements (CMOD), Δu. To overcome the limitation of knife-edge, contact points sensors, the non-contact digital image correlation (DIC) technique was used for evaluating the full-field displacement field on the surface of the sample. DIC analyses were performed through the *Ncorr* algorithm modified via an in-house made MATLAB routine (Ref 37). Two small rectangular regions of interest (ROIs), as shown in Fig. 3, were selected for computing horizontal u and vertical v displacements. The displacement vector of each notch edge was obtained by evaluating the mean values of the data calculated in a small range of selected points of ROIs (Ref 38).

3. Results and Discussion

3.1 Microstructural Analysis

Polished samples were observed in the scanning electron microscope at different magnifications (see Fig. 4, 5, and 6). The M100 and K790 samples presented a microstructure made of irregular and flak-shaped grains, having an average size of 1.40 and 1.09 μm, respectively. K95T15, on the other hand, is characterized by a coarser microstructure, with irregular and round-shaped grains having a mean size of 7.30 μm. Since the alumina powders used to manufacture the sample were from the same batch of K790, and the processing conditions were similar for all three types of sintered bulks, the difference in the microstructure could be ascribed to the addition of the titanium diboride with the starting mixture.

The lower processing conditions adopted to fabricate the samples influenced the final microstructure obtained. Higher processing temperature, around 1600 °C and dwell time, usually adopted in the hot-pressing sintering are claimed as the reason for the grain growth by Xu et al. (Ref 39), which measured a grain size of 6 μm after HP sintering starting from 2.9 μm alumina powders. In the present investigation, the lower temperature and holding time prevented the coarsening of the microstructure and the formation of equiaxed grains. It is clearly visible in the M100 and K790, where small anisotropic

grains with a high aspect ratio, approximately equal to 7. Some round-shaped equiaxed grains are still visible within the microstructure in both samples; those local variations can be the cause of the fluctuations in the response of the materials to the nano-indentation test. Microscopic pores and voids are also visible within the microstructure of both samples. They can be due to the presence of gases derived from the reaction of the residual oxygen with the impurities and remained entrapped within the powders during the consolidation and cooling (Ref 39).

K95T15 sample presents a coarse microstructure, characterized by grains having a hexagonal shape, which allows a higher degree of compaction between adjacent grains. Some elongated grains having a high aspect ratio are also visible in the microstructure (see Fig. 6). Those are common in sintered alumina and should be avoided because they are prone to form residual porosities at their boundaries. However, it has been also observed that such microstructures are potentially beneficial for the mechanical properties, leading to an increase in the crack resistance. The addition of a second phase usually leads to a refinement of the microstructure and higher densification (Ref 28); however, in the present case, the K95T15 sample has a relatively high level of porosities. This agrees with the observations of Rabiezadeh et al. (Ref 27), who detected that Al_2O_3/ TiB_2 composite manufactured by hot pressing at 1200 °C was not fully densified, while higher temperatures, around 1400-1500 °C enhance diffusion mechanisms and the densification, decreasing the number of pores. The addition of the TiB_2 within the alumina without other sintering additives may be detrimental to the sintering of the composite, resulting in a reduced relative density of the sintered bulk, even lower than 95%. That behavior is highly sensitive to the percentage of titanium diboride: the higher the amount of second-phase particles, the lower the densification level achievable (Ref 27). In the present case, those effects are mitigated by the action of the external pressure and the current, which favor the compaction, and by the relatively low amount of TiB_2 used in the mixture of powders.

The XRD spectra of the three different samples are shown in Fig. 7. The K790 and M100 samples show the typical spectrum of the α- Al_2O_3. Therefore, the only phase present in these samples was the corundum, in agreement with bulk obtained with spark plasma sintering process at the sintering temperatures between 1200 and 1400 °C. Slight variations in peak intensities and the broadening of the peaks can be ascribed to the sintering process (Ref 1, 25). In the K95T15 sample spectrum, it is possible to note the disappearance of the peak at a 2theta angle equal to 35°, which is present in the reference corundum, and a higher intensity for the peak at a 2theta angle of 38°. These variations can be ascribed to the additional TiB_2 phase, used during the sintering process (Ref 27, 32).

No other species, distinct from alpha-alumina and titanium diboride, were found in the K95T15 sample, even though some compounds produced by the reaction of alumina with the other elements could be expected. $Al_{18}B_4O_3$ and Ti_2O_3 might be formed according to the reactions:

$$9Al_2O_3 + TiB_2 \rightarrow 9Al_2O + 2Ti_2O_3 + 4B_2O_3$$

$$9Al_2O + 2B_2O_3 + 9O_2 \rightarrow Al_{18}B_4O_{33}$$
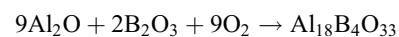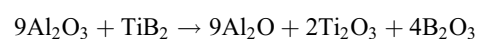
The formation of $Al_{18}B_4O_3$ usually occurs due to the presence of entrapped air inside the green compact and the
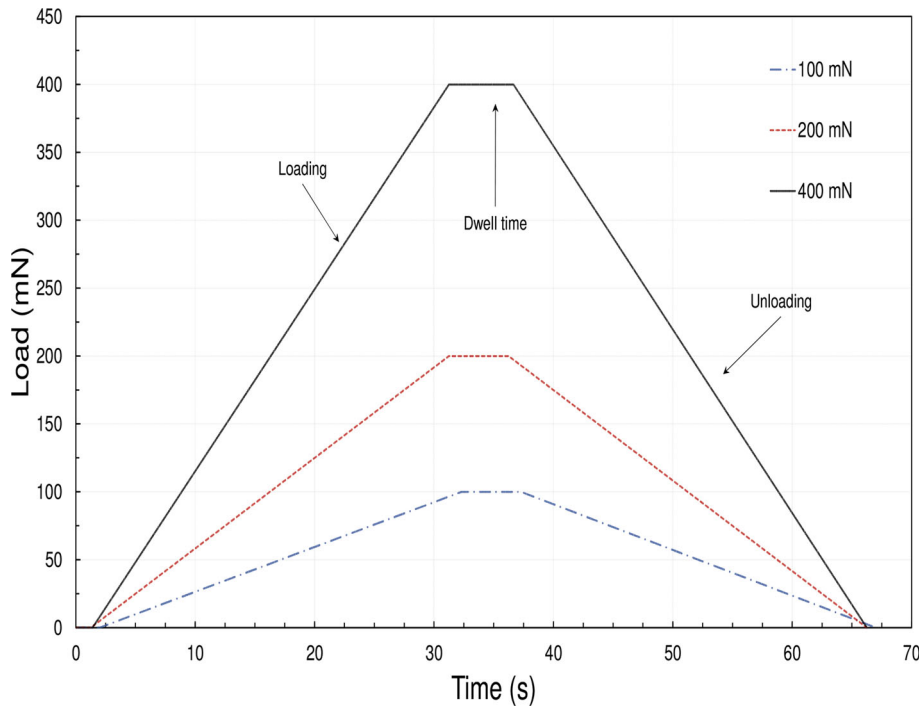
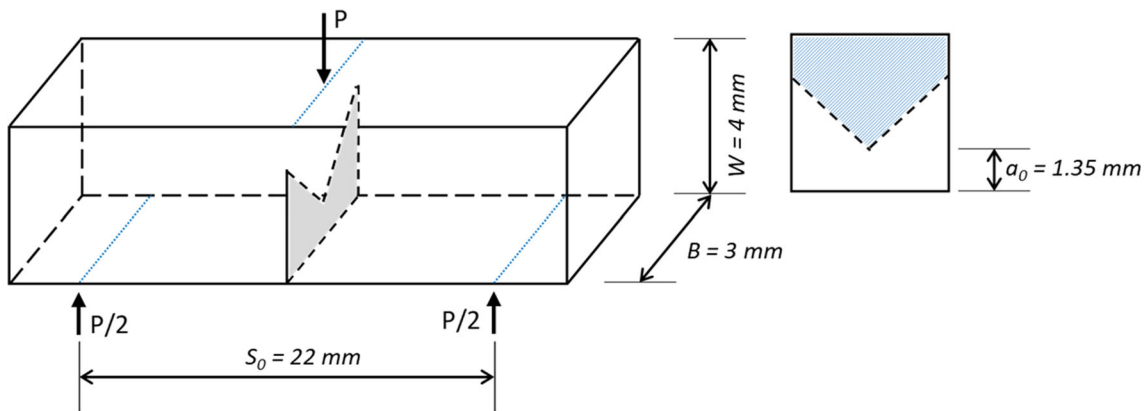**Fig. 1** Load-time curves at different peak loads

Fig. 2 Chevron notch beam (CNB) specimen in three-point flexure loading condition

consequent reaction of the oxygen with the other constituents (Ref 27). In the case of the P^2C process, since the sintering was conducted under vacuum conditions, the formation of such compounds is prevented. The lower peaks of titanium diboride and the absence of the titanium oxide in the XRD spectrum of the K95T15 specimen, with respect to what is reported in the literature (Ref 27, 40), can also be ascribed to the limited amount of TiB_2 added in the alumina particles; thus, they can be below the limits of detection or confused with the pattern background.

3.2 Nano-Hardness Tests

Nano-indentations at loads of 100, 200, and 400 mN were conducted on the three types of compacted alumina ceramics. Typical displacement-load curves from the nano-indentation test are reported in Fig. 8 for the K95T15 sample tested for all three maximum loads, while Table 1 reports the value of Young's modulus and hardness of all three samples at different maximum loads.

The maximum indentation depths for the three test conditions are shown in Fig. 9. The values of the penetration depth obviously increase with the maximum load set during the indentation tests: average values of approximately 0.1, 0.7, and 1 μm were measured for the indentions made using maximum loads of 100, 200, and 400 mN, respectively.

The three sintered ceramics showed values very close to each other, especially samples K95T15 and M100, while sample K790 registered the lowest values for all test loads. Sample M100, in addition, is characterized by a more pronounced scattering of the measurements. Besides that, no significant variations can be observed in the indentation depth between the three samples. Indeed, the average values fall within the ranges of the measurements of the samples, which overlap each other. This behavior is reflected by the values of the hardness measured in the three materials.
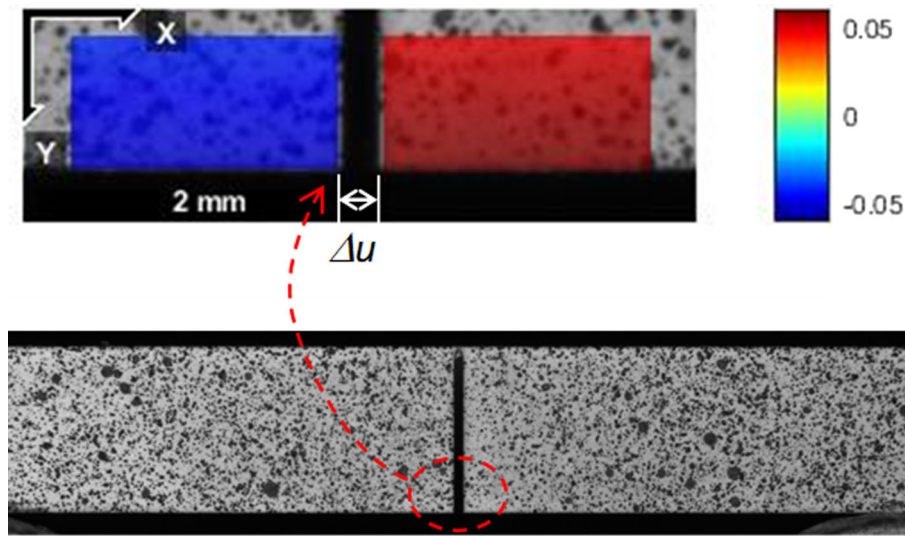
Fig. 3 ROIs location for displacements measurement
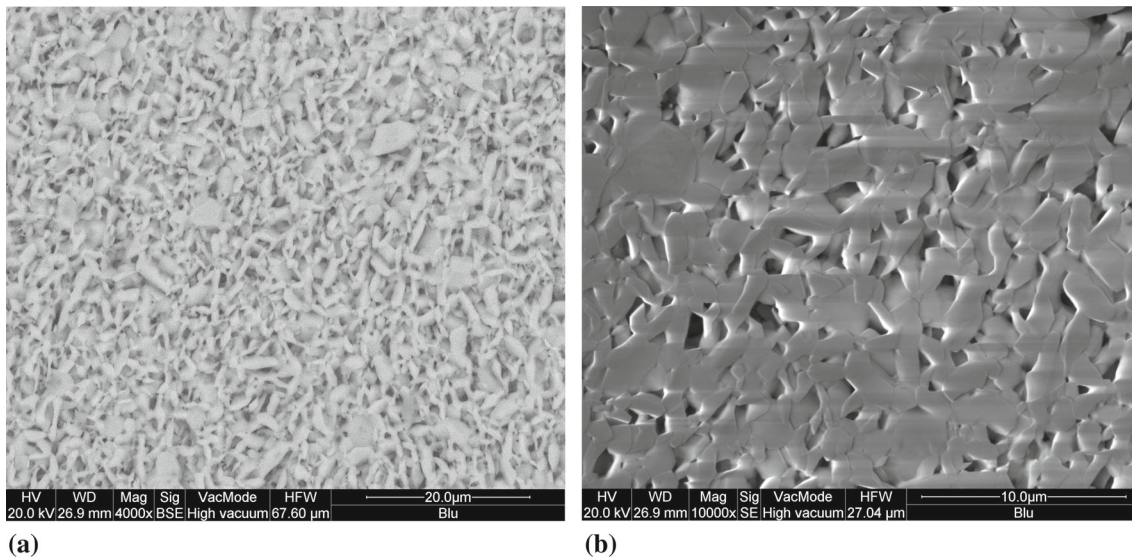

(a)

(b)

Fig. 4 Microstructure of K790 samples at different magnification

The hardness value was calculated from the load-depth curve according to the equation proposed by Oliver and Pharr (Ref 35). The mean value of hardness from all the tests was found equal to 21.2 GPa for sample K95T15, 23.4 GPa for sample K790, and 19.2 GPa for the sample M100, with a limited scattering of the data characterized by a standard deviation of approximately 1.0 GPa for all test cases. The values observed are close to those reported by other authors relative to pure alumina sintered by hot pressing at 1400-1600 °C, which claimed values of the hardness in the range of 20-24 GPa (Ref 25, 41, 42).

The hardness is strongly influenced by the grain size, increasing as the latter decreases. Values of 20-23 GPa were claimed by authors for sintered alumina with grains having a mean size of 0.6 μm (Ref 25, 43), while it can drop to 15 GPa in the case of micrometer microstructure. The dependence of hardness on the dimension of the grains indicates a marked sensitivity toward the processing conditions, temperature and holding time first, and subsequently pressure and heating rate.

The grain growth process is, indeed, thermally activated: processing temperature above 1250 °C leads to an exponential increase in the grain size of spark plasma sintered bulks even for reduced holding time, with a consequent drop of hardness. Reduction from 20 to 16 GPa was registered for sintered alumina processed at 1200 °C and 1500 °C. Conversely, for temperatures below 1250 °C, grain growth is prevented or very limited (Ref 25). Processing time has a similar influence: higher holding time allows for the establishment of grain-boundary diffusion mechanisms that promote the growth of the grains during the compaction (Ref 25). The average values of hardness are also influenced by the presence of TiB_2. Titanium diboride particles were expected to increase the hardness, due to the higher value of the pristine materials, which is reported above 30 GPa. Therefore, the higher the amount of TiB_2 within the mixture of powders the higher the overall hardness of the sintered bulk. In the present case, being its percentage limited to only 5%, a slight increase is reasonably expected.
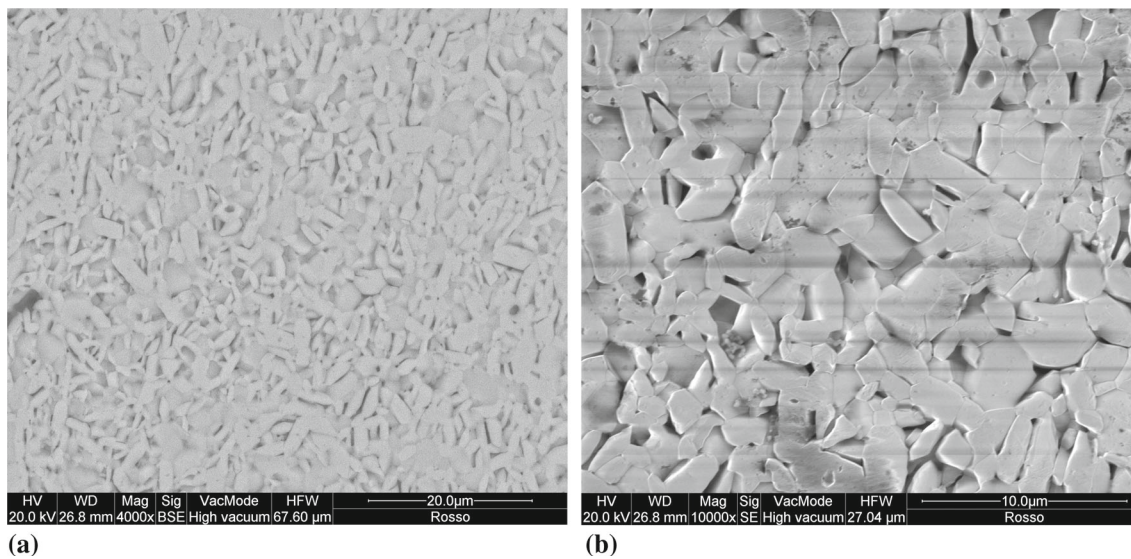
Fig. 5 Microstructure of M100 samples at different magnification
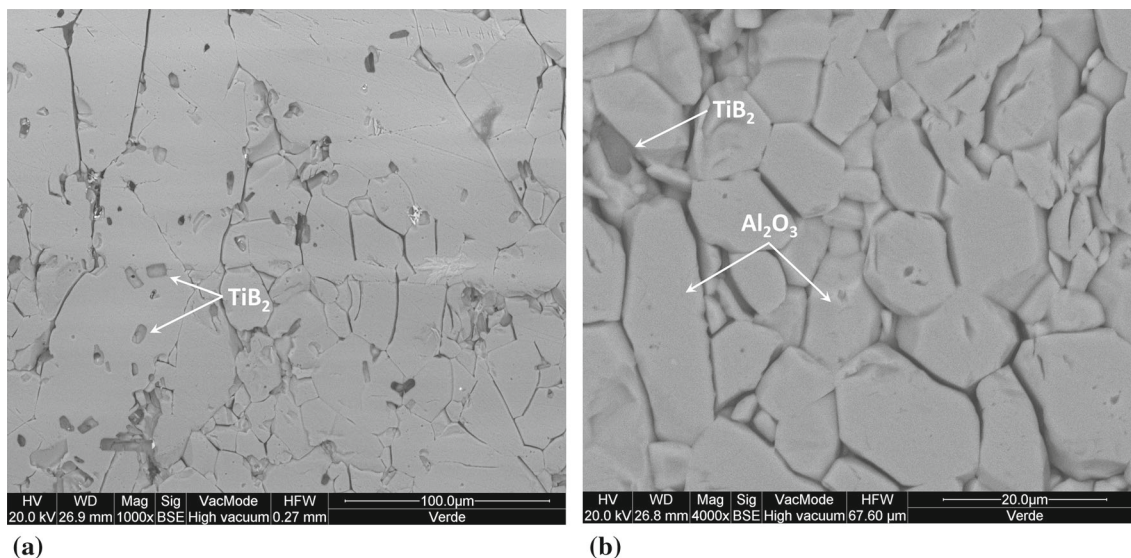

Fig. 6 Microstructure of K95T15 samples at different magnification

The Oliver and Pharr approach was adopted also for the calculation of the Young's modulus of the alumina ceramics from the load-depth curves (Ref 35). The elastic modulus of the three samples was found in the range between 500 and 580, 532-620, and 430-550 GPa for K95T15, K790, and M100, respectively. Increasing values were estimated with the increase in test load. The width of the range is in order of 100 GPa, which is common for sintered alumina. The average values were slightly above those observed in hot-pressed alumina bulks, which were approximately 460 GPa (Ref 41, 44), except for the M100 which showed the lowest value around 410 GPa, but also a wide scattering with a peak measurement of approximately 690 GPa (see Table 1). It is related to the wide variation in the maximum indentation depth registered on the sample at the maximum load of 200 mN (see Fig. 9).

The average elastic modulus E measured in the alumina bulks sintered by the P^{2}C process was equal to approximately 530, 560, and 490 GPa for samples K95T15, K790 and M100,

respectively. The values, as mentioned above, are approximately 10-20% higher than the values observed in commercial polycrystalline alumina (Ref 44). As described before, the elastic modulus depends on the indentation behavior of the material and is sensitive to local microstructural features. Therefore, the scattering in data from nano-indentation can be ascribed to the variations in microstructure, like the presence of second-phase inhomogeneities in the K95T15 or of grain with different shapes in the M100 and K790 sample, and the residual porosity (see Fig. 4 and 5) (Ref 45).

The values of hardness and Young modulus were found to vary for each type of alumina sample with the maximum load adopted in the nano-indentation test. The fluctuations can be due to the kinetic effects resulting from the adoption of the different load rates (from 200 up to 800 mN/min). The tests, indeed, are conducted up to the prescribed maximum loads within the same time: the distinct rates lead to different penetration depths at the same value of the load, which results

in different values of hardness and elasticity modulus (Ref 41). It also explains the discrepancy with the published results, influenced by the different loading conditions and the maximum loads adopted.

By analyzing the load-indentation curves is possible to estimate the degree of elastic recovery, Δe. It is calculated from the unloading segment of each curve after the measurement of the maximum penetration, h_{max}, and the residual depth, h_p, according to:
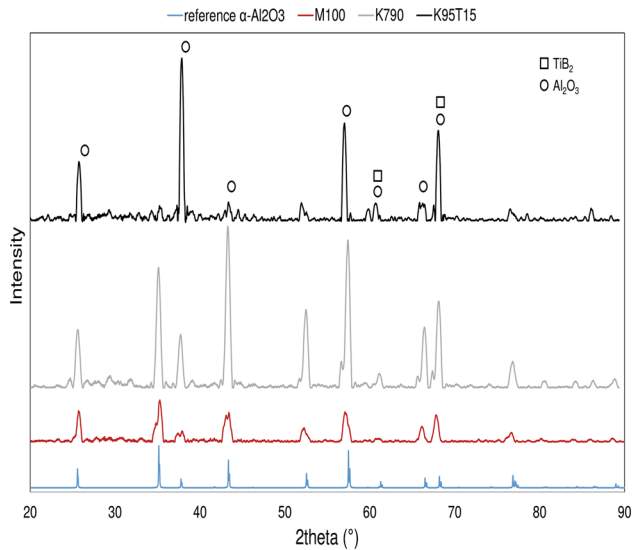
$$\Delta e = (h_{max} - h_p)/h_{max} \qquad (Eq\ 2)$$
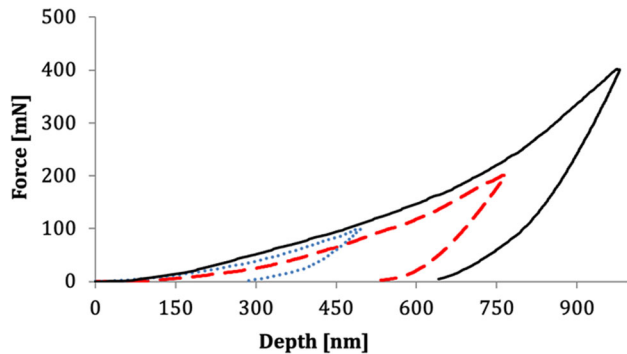
In the present experimentation, values of approximately 0.34 were found for all types of sintered, with small differences between them, which were within the experimental error. High values of the elastic recovery (a value of 0.124 was claimed for the hot-pressed pure alumina (Ref 42)) indicate the capability of the materials to store strain energy and accommodate the local stresses generated by the indenter, without the occurrence of extensive cracking. The usage of a small amount of titanium boride as a sintering aid, although it showed a marked effect on grain size, tenacity, and mechanical properties, had no significant influence on the residual plastic deformation.

All samples showed the typical hysteresis cycle of the load-indentation displacement curve characteristic of the materials having the elastic–plastic behavior. Some of the indentions showed discontinuities during the loading segment, called "pop-ins". These discontinuities appear as a sudden increase in the displacement at fixed load, like localized creep events (Fig. 10). The pop-ins are related to fracture events that occurred under the action of the indenter around the area interested by the indentations. Usually, these fractures correspond to a mixture of inter- and intra-granular cracks (see Fig. 6a). By observing the graph of one of the indentations, the discontinuities occurred between 923 and 940 nm at a load of 282 mN. Roughly the deformation work associated with the displacement was 4.6 nJ. Following the approach adopted by Twigg et al. (Ref 42), it is possible to estimate that the energy accumulated could be able to produce a fracture surface of approximately 780 μm^2 (fracture energy in α-alumina for the rhombohedral $(01\bar{1}2)$ and prismatic planes $(10\bar{1}0)$ (1010) were found in the range between 6 and 7.5 J/m^2 (Ref 46)), which corresponds to a theoretical circular crack of approximately 31 μm. Cracks observed in the samples are roughly ten or 15 μm, consistent with those that can be generated by pop-in events.

Pop-in events are less pronounced in the sample K95T15 at all three load conditions and the loading segments present very few discontinuities, which can be associated with a reduced tendency to form microcracks. The presence of the secondary phase within the alumina matrix can promote some toughening crack mechanisms, like crack deflection of branching, due to the interactions of the crack with the titanium diboride particle (Ref 31).

3.3 Fracture Toughness

Figure 11 reports the load–displacement curves registered during the CNB tests. Three measurements were conducted for each sample.

Figure 12 reports the representative load-versus-CMOD curves acquired during the fracture tests.

All the specimens exhibited a planar and smooth crack propagation up to the final rupture pointed out by the overall smooth trend in the load-CMOD curves. First, the increase in

Table 1 Nano-hardness and Young's modulus for the P²C alumina samples

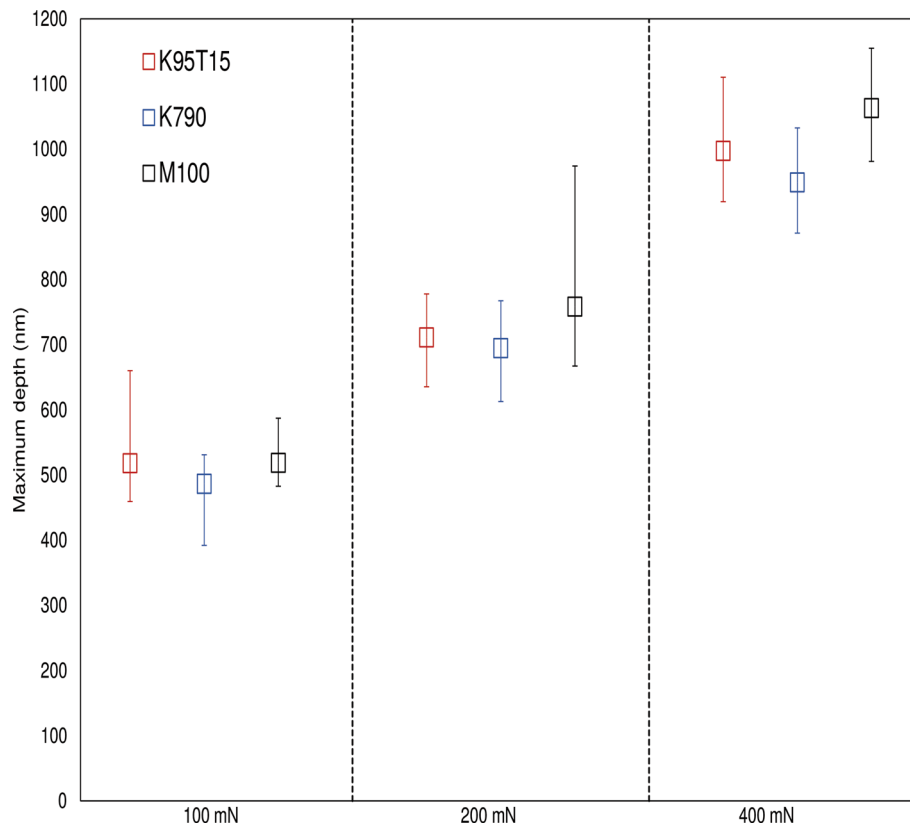| Maximum load	K95T15		K790		M100	
	Hardness, GPa	Young modulus, GPa	Hardness, GPa	Young modulus, GPa	Hardness, GPa	Young modulus, GPa
100 mN	20.01 ± 6.55	503.67 ± 77.45	23.85 ± 9.04	532.28 ± 129.17	20.23 ± 4.56	432.09 ± 20.22
200 mN	21.26 ± 2.91	576.31 ± 349.94	22.29 ± 4.22	540.57 ± 120.69	18.83 ± 5.75	547.68 ± 106.73
400 mN	22.44 ± 5.70	519.74 ± 31.30	24.10 ± 3.60	618.72 ± 86.91	18.52 ± 2.06	504.39 ± 91.93

Fig. 9 Maximum indentation depth

loading is nearly linear as CMOD increases (linear elasticity stage). After the reach of the peak load value, the decrease in load occurs almost slowly. Therefore, an almost stable test state can be highlighted. Furthermore, DIC analyses showed that the displacements of the notch mouth edges were almost symmetric with respect to the crack plane. Microscopic analysis of the post-mortem specimens' fracture surfaces is shown in Fig. 13. The images of the fracture surface of CNB samples confirm the crack onset at the vertex of inserted chevron notch.

The maximum load was carried out by the tests on the samples made of K95T15, which reached about 24% and 27% greater forces than K790 and M100 specimens, respectively (see Fig. 11). The repeatability of the test results is indicated by the coefficient of variation, obtained as described in the ISO 5725-2 standard. Specimens made of M100 highlighted less data dispersion.

The measured fracture toughness of the analyzed samples is reported in Table 2.

The values are close to those obtained from the sintering of amorphous Al_2O_3 powders by using the SPS process, which is claimed to be around 4.5 MPa m$^{1/2}$, and slightly higher than those obtained by hot pressing of pure alumina which is approximately 4.0 MPa m$^{1/2}$ (Ref 31, 47). The relatively high values of fracture toughness were obtained using lower operating temperature and holding time than those usually adopted in the other sintering processes, usually around 1400 and 1600 °C, if not above (Ref 31, 47). The less demanding parameters prevented excessive grain growth. The fracture toughness of M100 and K790 can be ascribed to morphological and microstructural factors: the elongated grains with a high aspect ratio may exert a reinforcing action within the Al_2O_3
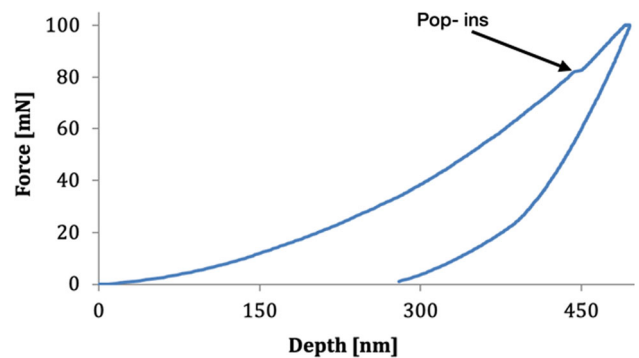

Fig. 10 Load-indentation depth showing "pop-in" discontinuity (Sample M100, maximum load 400mN).Fig. 10. Load-indentation depth showing "pop-in" discontinuity (Sample M100, maximum load 400mN)

matrix and cause an improvement in the fracture toughness (Ref 48). The abnormally grown grain and the rod-shape morphology observed in the K790 and M100 (see Fig. 4 and 5), foster the establishing of crack deflection and bridging effect as main toughening mechanisms, which slow down the propagation of the cracks. In monolithic alumina, the main fracture mechanism is associated with the inter-granular fracture with crack propagating through the grain boundaries. In sintered alumina, characterized by equiaxed grains having a hexagonal shape and by high densification (> 99%), the crack propagation path is the shortest one and the most uniform due to the closeness of adjacent grains and their high compaction degree. Conversely, in alumina bulks with pronounced elon-
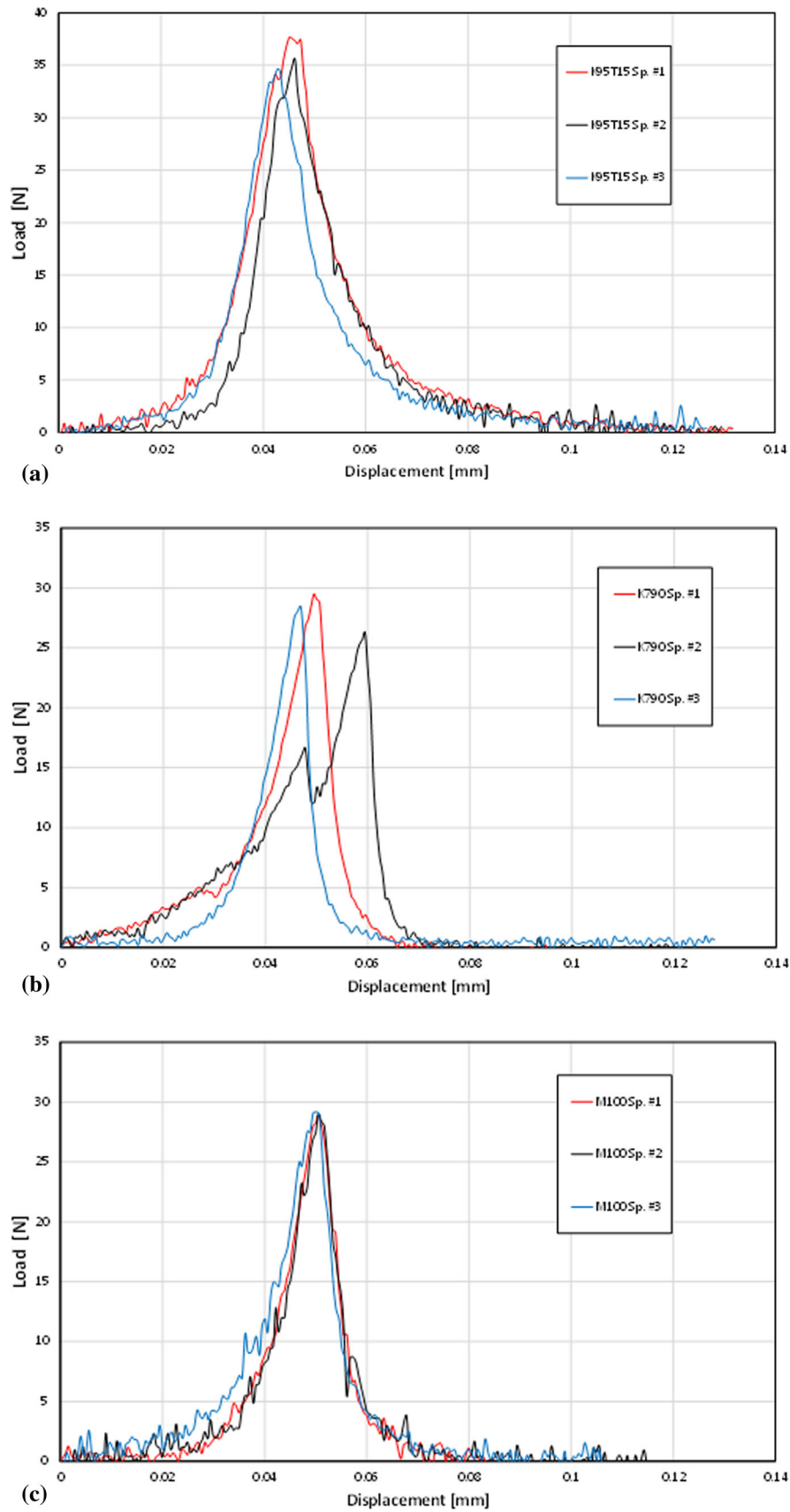
Fig. 11 Load-displacement curve for specimens: (a) K95T15; (b) K790; (c) M100

gated grains, the crack propagation path generated by the abnormal growth deviates from a uniform trajectory and becomes longer, slowing down the evolution of the fracture (Ref 39). Kolvar et al. (Ref 48) also demonstrated that a coarse microstructure has a similar effect on the strength and the stability of the ceramic leading to an increase in the tortuosity of the crack path. However, excessive grain growth, obtainable by adopting high temperature or holding time, can be detrimental to the other mechanical properties. Proper tuning of the sintering process is paramount to achieving a good balance between the performance of the manufactured product.

The use of additives, called "seeds", within the alumina powders, like titanium dioxide (Ref 49, 50), aluminate (Ref 51), zirconia or titanium carbide (Ref 47) allows to modify the final microstructure and promote the crack deflection toughening mechanism. As far as the K95T15 specimen, the fracture toughness reached 5.43 MPa·m$^{1/2}$, which is higher than the other specimens. The improved strength can be ascribed to two factors: the increase in grain size (as mentioned above) and the incorporation of the second-phase particles, with the consequent interactions between the crack and the hard titanium diboride.

The strength of alumina-based ceramics depends, indeed, on the grain size (GS) (Ref 52). For polycrystalline ceramics, like alumina or rutile, the fracture toughness overalls increase with GS, but its trend presents a nonlinear dependence at a small size, a plateau for middle-range grains, and, after the maximum, it decreases with the increase in the grain dimensions. Alumina ceramics having grains size below 10 μm experience the fastest toughening with the grain size, due to the occurrence of crack bridging phenomena (Ref 53, 54). In the present case, the addition of titanium diboride in the K95T15 caused the increase in grain size from approximately 1 μm observed in the K790 and M100 samples to 7 μm, resulting in the observed higher fracture strength: larger grains, indeed, determine a higher clamping force on the crack surfaces derived by compressive stress from thermal expansion and, therefore, the material is able to resist a higher crack opening displacement before the failure.

On the other side, the introduction of second-phase particles to the brittle matrix leads to an increase in strength by enhancing the crack bowing toughening mechanism. Those particles act, indeed, as a barrier to the crack advance slowing its planar propagation (Ref 55). Remarkable improvement in the fracture toughness was observed already in the alumina composite matrix with a low percentage of TiB$_2$ reinforcement: values between 5.5 and 6.5 MPa m$^{1/2}$ were observed for 5% of titanium diboride with respect to the 4.0 MPa m$^{1/2}$ of the pure alumina (Ref 31). Indeed, TiB$_2$ contributes to the increase in the fracture toughness due to crack deflection and crack bridging mechanisms around the titanium diboride particles (Ref 27, 56). On the other hand, a further increase in the amount of reinforcement particles did not show a positive influence lowering the fracture toughness to a plateau of 5.0-5.5 MPa m$^{1/2}$. The beneficial effect can be also ascribed to the size of the particles used in the sintering of alumina powders. Indeed, it has been observed that fracture toughness of sintered alumina is dependent on the dimensions of the titanium diboride TiB$_2$ particles, where the use of micrometer powders in the order of 3-6 μm provides the highest increase in the fracture toughness (Ref 57), while nanometer particles have a lower or null impact regardless the amount of reinforcing particle used (Ref 30). In
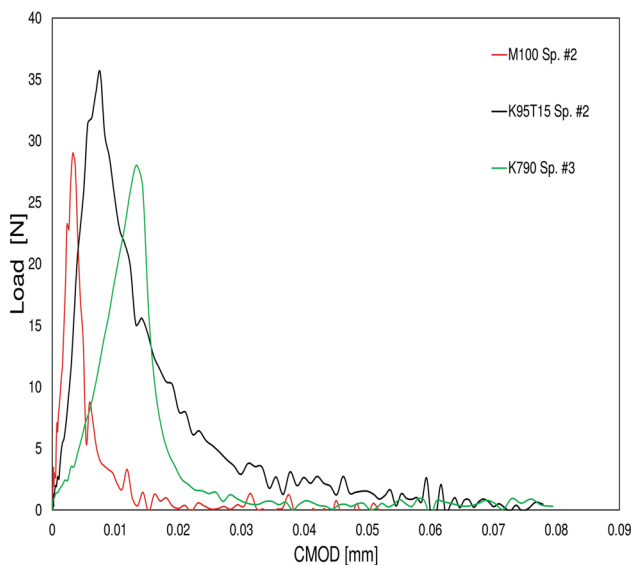

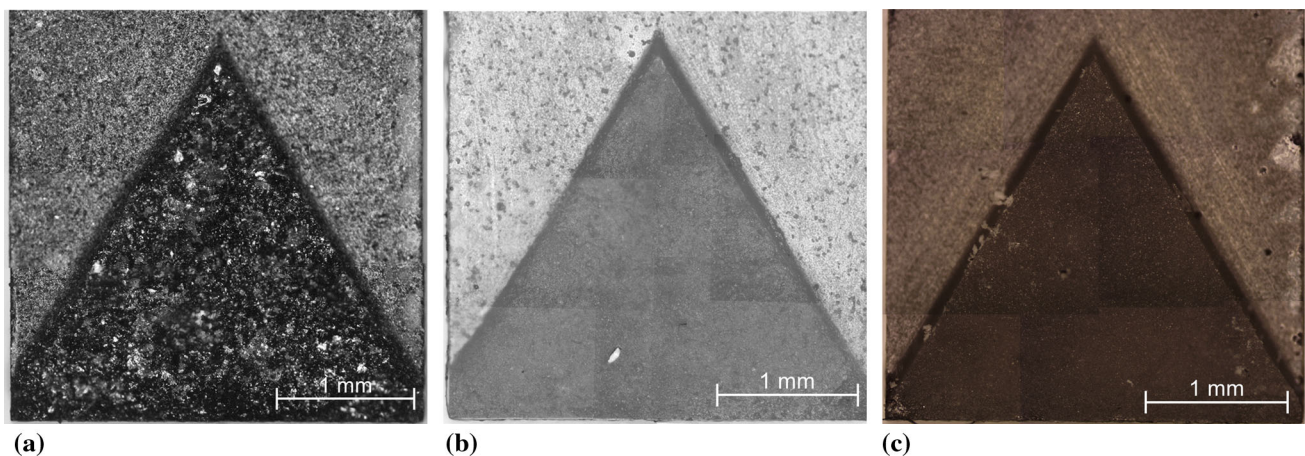**Fig. 12** Representative Load vs. CMOD curves for K95T15, K790 and M100 specimens

Fig. 13 Top view of a coplanar crack of P2C specimens: (a) K95T15, (b) K790, (c) M100

Table 2 Experimental fracture toughness K_{Ivb} [$MPa \bullet \sqrt{m}$]

Material	K95T15	K790	M100
Specimen #1	5.70	4.54	4.38
Specimen #2	5.38	4.00	4.40
Specimen #3	5.22	4.26	4.34
Mean value	5.43	4.27	4.37
Standard deviation	0.20	0.22	0.02
Coefficient of variation CV, %	3.65	5.14	0.54

the present case, the titanium diboride particles had an average size of approximately 8 μm (see Fig. 6).

The difference in the values observed for the alumina/TiB$_2$ ceramic produced by the P^{2}C process can be partly ascribed to the different measurement method adopted, which has a significant influence on the measured values and partly to the process itself and the parameter adopted.

4. Conclusions

Alumina-based ceramics were produced by using plasma pressure compaction sintering process. Two pure alumina ceramics and Al$_2$O$_3$ matrix reinforced with TiB$_2$ particles composite were fabricated. Microstructure, composition, and mechanical properties of the three samples were estimated. Based on the conducted investigation, the following remarks can be drawn:

1. Alumina powders and titanium diboride plus alumina mixture were successfully consolidated by using the P^{2}C process.
2. Microstructural observations of the samples revealed a heterogeneous microstructure, consisting of micrometer grains having elongated rod-like shape, alternated with rounded grains, and microscopic pores and voids for K790 and M100 samples. The K95T15 showed a coarser microstructure, characterized by hexagonal-shaped grains that allowed more densification and dispersed titanium diboride particles at the grain boundaries. The x-ray diffraction revealed that the main constituent of the sintered ceramics is the alpha Al$_2$O$_3$ phase. Some peaks in the K95T15 sample can be ascribed to the presence of TiB$_2$ particles.
3. The nano-hardness values ranged from 18 up to 23 GPa, and the elastic modulus spanned between approximately 500 and 630 GPa. They are consistent with alumina ceramics obtained with Spark Plasma Sintering. All samples showed a wide scattering of the data from the nano-indentation. This can be ascribed to the highly heterogeneous microstructure observed in all the samples as well as to the test conditions.
4. The fracture toughness of K790 and M100 was equal to approximately 4.3 MPa m$^{1/2}$, consistently with the sintered alumina obtained by dry pressing techniques. The K95T15, conversely, showed an increase in the fracture toughness, which reached 5.4 MPa m$^{1/2}$. The observed increment in fracture resistance can be ascribed to the occurrence of toughening mechanisms, such as crack bridging and crack deflection, triggered by the presence of titanium diboride particles. The grain growth may also have influenced the increment of fracture toughness. The evaluation of CMOD parameter by DIC analysis provided useful information on the stability and repeatability of fracture tests
5. In summarizing, P^{2}C proved to be a suitable alternative to produced alumina ceramics having high properties with less demanding processing conditions, compared to the conventional dry pressing techniques or the SPS process. P^{2}C is also able to successfully produce alumina matrix composites reinforced with titanium diboride. Potential future development may involve the assessing of P^{2}C capability with higher percentages of TiB$_2$ particles or other secondary hard phases.

References

1. V. An, A. Khasanov and C. de Izarra, Spark Plasma Sintering of Alumina Nanopowders Produced by Electrical Explosion of Wires, *Springerplus*, 2015, **4**(1), p 581
2. G.C. Wei, Transparent Ceramic Lamp Envelope Materials, *J. Phys. D Appl. Phys.*, 2005, **38**(17), p 3057–3065
3. A.V. Nartova, A.V. Bukhtiyarov, R.I. Kvon, and V.I. Bukhtiyarov, The Model Thin Film Alumina Catalyst Support Suitable for Catalysis-Oriented Surface Science Studies, *Appl. Surf. Sci.*, 2015, **349**, p 310–318
4. X. Mao, S. Shimai, M. Dong, and S. Wang, Gelcasting and Pressureless Sintering of Translucent Alumina Ceramics, *J. Am. Ceram. Soc.*, 2008, **91**(5), p 1700–1702
5. S. Deville, J. Chevalier, G. Fantozzi, J.F. Bartolomé, J. Requena, J.S. Moya, R. Torrecillas, and A. Dìaz, Low-Temperature Ageing of Zirconia-Toughened Alumina Ceramics and Its Implication in Biomedical Implants, *J. Eur. Ceram. Soc.*, 2003, **23**(15), p 2975–2982
6. W.E. Lee and M. Rainforth, *Ceramic Microstructures Property Control by Processing*, 1st edn. (Springer Netherland, 1994)
7. D. Salamon and Z. Shen, Pressure-Less Spark Plasma Sintering of Alumina, *Mater. Sci. Eng. A*, 2008, **475**(1–2), p 105–107

8. C. Manière, L. Durand, A. Weibel, and C. Estournès, Spark-Plasma-Sintering and Finite Element Method: From the Identification of the Sintering Parameters of a Submicronic α-Alumina Powder to the Development of Complex Shapes, *Acta Mater*, 2016, **102**, p 169–175

9. Y. Aman, V. Garnier and E. Djurado, Influence of Green State Processes on the Sintering Behaviour and the Subsequent Optical Properties of Spark Plasma Sintered Alumina, *J. Eur. Ceram. Soc.*, 2009, **29**(16), p 3363–3370

10. R.L. Coble and W.D. Kingery, Effect of Porosity on Physical Properties of Sintered Alumina, *J. Am. Ceram. Soc.*, 1956, **39**(11), p 377–385

11. P. Angerer, E. Neubauer, L.G. Yu, and K.A. Khor, The Spark-Plasma-Sintering (SPS) Process in Comparison with Various Conventional Compaction Methods, in *Pulse Electric Current Synthesis and Processing of Materials*, ed. By Z.A. Munir, M. Ohyanagi, M. Tokita, M. Khor, T. Hirai, U. Anselmi-Tamburini (Wiley, Hoboken, NJ, USA, 2011), pp. 23–35

12. R.K. Bordia, E.A. Olevsky (eds.), *Advances in Sintering Science and Technology* (Wiley, Hoboken, NJ, USA, 2009)

13. M. Suarez, A. Fernandez, J.L. Menendez, R. Torrecillas, H. U., J. Hennicke, R. Kirchner, and T. Kessel, Challenges and Opportunities for Spark Plasma Sintering: A Key Technology for a New Generation of Materials, in *Sintering Applications*, (InTech, 2013)

14. J. Monnier, Y. Champion, L. Perrière, B. Villeroy, and C. Godart, Spark Plasma Sintering and Hydrogen Pre-Annealing of Copper Nanopowder, *Mater. Sci. Eng. A*, 2015, **621**, p 61–67

15. Z. Zhao, V. Buscaglia, P. Bowen, and M. Nygren, Spark Plasma Sintering of Nano-Crystalline Ceramics, *Key Eng. Mater.*, 2004, **264–268**, p 2297–2300

16. S.W. Wang, L.D. Chen, and T. Hirai, Densification of Al$_2$O$_3$ Powder Using Spark Plasma Sintering, *J. Mater. Res.*, 2000, **15**(4), p 982–987

17. L. Gao, J.S. Hong, H. Miyamoto, and S.D.D.L. Torre, Bending Strength and Microstructure of Al2O3 Ceramics Densified by Spark Plasma Sintering, *J. Eur. Ceram. Soc.*, 2000, **20**(12), p 2149–2152

18. D. Ghosh, G. Subhash, R. Radhakrishnan, and T.S. Sudarshan, Scratch-Induced Microplasticity and Microcracking in Zirconium Diboride-Silicon Carbide Composite, *Acta Mater.*, 2008, **56**(13), p 3011–3022

19. B.R. Klotz, K.C. Cho, and R.J. Dowding, Sintering Aids in the Consolidation of Boron Carbide (B$_4$C) by the Plasma Pressure Compaction (P$_2$C) Method, *Mater. Manuf. Process.*, 2004, **19**(4), p 631–639

20. D. Ghosh, G. Subhash, T.S. Sudarshan, R. Radhakrishnan, and X.-L. Gao, Dynamic Indentation Response of Fine-Grained Boron Carbide, *J. Am. Ceram. Soc.*, 2007, **90**(6), p 1850–1857

21. M.G. Bothara, P. Vijay, S.V. Atre, S.J. Park, R.M. German, T.S. Sudarshan, and R. Radhakrishnan, Design of Experiment Approach for Sintering Study of Nanocrystalline SiC Fabricated Using Plasma Pressure Compaction, *Sci. Sinter.*, 2009, **41**(2), p 125–133

22. B.G. Ravi, O.A. Omotoye, T.S. Srivatsan, M. Petrorali, and T.S. Sudarshan, The Microstructure and Hardness of Silicon Carbide Synthesized by Plasma Pressure Compaction, *J. Alloys Compd.*, 2000, **299**(1–2), p 292–296

23. T.S. Srivatsan, B.G. Ravi, A.S. Naruka, L. Riester, M. Petraroli, and T.S. Sudarshan, The Microstructure and Hardness of Molybdenum Powders Consolidated by Plasma Pressure Compaction, *Powder Technol.*, 2001, **114**(1–3), p 136–144

24. F. Rubino, M. Pisaturo, A. Senatore, P. Carlone, and T.S. Sudarshan, Tribological Characterization of SiC and B4C Manufactured by Plasma Pressure Compaction, *J. Mater. Eng. Perform.*, 2017, **26**(11), p 5648–5659

25. Z. Shen, M. Johnsson, Z. Zhao, and M. Nygren, Spark Plasma Sintering of Alumina, *J. Am. Ceram. Soc.*, 2002, **85**(8), p 1921–1927

26. T. Nallusamy and S. Vijayakumar, High-Temperature Stability of Titanium Boride Reinforced Alumina-Silicon Carbide Based Composite, *Silicon*, 2021, **13**(4), p 1087–1095

27. A. Rabiezadeh, A. Ataie, and A.M. Hadian, Sintering of Al$_2$O$_3$-TiB$_2$ Nano-Composite Derived from Milling Assisted Sol-Gel Method, *Int. J. Refract. Met. Hard Mater.*, 2012, **33**, p 58–64

28. T.S. Srivatsan, G. Guruprasad, D. Black, R. Radhakrishnan, and T.S. Sudarshan, Influence of TiB2 Content on Microstructure and Hardness of TiB2–B4C Composite, *Powder Technol.*, 2005, **159**(3), p 161–167

29. A.R. Keller and M. Zhou, Effect of Microstructure on Dynamic Failure Resistance of Titanium Diboride/Alumina Ceramics, *J. Am. Ceram. Soc.*, 2003, **86**(3), p 449–457

30. D.-S. Park and B.-D. Han, Properties of Hot Pressed Alumina-Titanium Diboride Particulate Composites, *Korean J. Ceram.*, 1998, **4**(3), p 227–230

31. J. Liu and P.D. Ownby, Enhanced Mechanical Properties of Alumina by Dispersed Titanium Diboride Particulate Inclusions, *J. Am. Ceram. Soc.*, 1991, **74**(1), p 241–243

32. T. Sato, Y. Sasaki, and I. Saeki, Influence of Processing Condition of Ti, Al, and B2O3 Mixed Powders on the Preparation of Al2O3–40.5 Mass % TiB2 Sintered Compact by HIP, *J. Ceram. Soc. Jpn.*, 2011, **119**(1390), p 502–506

33. J. Wachsmuth, R. Radhakrishnan, and T.S. Sudarshan, Effect of Pulsed Current on Reactively Synthesised TiB$_2$ Consolidated by Plasma Pressure Compaction, *Powder Metall.*, 2003, **46**(4), p 361–364

34. M.G. Bothara, S.V. Atre, S.-J. Park, R.M. German, T.S. Sudarshan, and R. Radhakrishnan, Sintering Behavior of Nanocrystalline Silicon Carbide Using a Plasma Pressure Compaction System: Master Sintering Curve Analysis, *Metall. Mater. Trans. A*, 2010, **41**(12), p 3252–3261

35. W.C. Oliver and G.M. Pharr, An Improved Technique for Determining Hardness and Elastic Modulus Using Load and Displacement Sensing Indentation Experiments, *J. Mater. Res.*, 1992, **7**(6), p 1564–1583

36. ASTM C 1421–18 - Standard Test Method for Determination of Fracture Toughness of Advanced Ceramics at Ambient Temperatures. in *Book of Standards* Vol. 15.01(American Society for Testing and Materials, West Conshohocken, PA, USA, 2018), pp. 641–672

37. H. Schreier, J.-J. Orteu, and M.A. Sutton, *Image Correlation for Shape, Motion and Deformation Measurements*, Springer, Boston, MA, 2009

38. J. Blaber, B. Adair, and A. Antoniou, Ncorr: Open-Source 2D Digital Image Correlation Matlab Software, *Exp. Mech.*, 2015, **55**(6), p 1105–1122

39. L. Xu, Z. Xie, L. Gao, X. Wang, F. Lian, T. Liu, and W. Li, Synthesis, Evaluation and Characterization of Alumina Ceramics with Elongated Grains, *Ceram. Int.*, 2005, **31**(7), p 953–958

40. S.H. Kenawy, Synthesis and Characterization of Aluminum Borate Ceramic Whiskers, *Int. J. Appl. Ceram. Technol.*, 2011, **8**(4), p 783–792

41. A. Krell and S. Schädlich, Nanoindentation Hardness of Submicrometer Alumina Ceramics, *Mater. Sci. Eng. A*, 2001, **307**(1–2), p 172–181

42. P.C. Twigg, F.L. Riley, and S.G. Roberts, Nanoindentation Investigation of Micro-Fracture Wear Mechanisms in Polycrystalline Alumina, *J. Mater. Sci.*, 2002, **37**(4), p 845–853

43. A. Krell, Load Dependence of Hardness in Sintered Submicrometer Al2O3 and ZrO2, *J. Am. Ceram. Soc.*, 1995, **78**(5), p 1417–1419

44. B. Dhakar, S. Chatterjee, and K. Sabiruddin, Measuring Mechanical Properties of Plasma-Sprayed Alumina Coatings by Nanoindentation Technique, *Mater. Sci. Technol. (U. K.)*, 2017, **33**(3), p 285–293

45. J.B. Wachtman, W.R. Cannon, and M.J. Matthewson, Elasticity, in *Mechanical Properties of Ceramics*, (Wiley, Hoboken, NJ, USA, 2009), pp 35–54

46. S.M. Wiederhorn, Fracture and Deformation of Alumina (Durham, North Carolina 27706, 1973)

47. M. Szutkowska, Fracture Toughness of Advanced Alumina Ceramics and Alumina Matrix Composites Used for Cutting Tool Edges, *J. Achiev. Mater. Manuf. Eng.*, 2012, **54**(2), p 202–210

48. D. Kovar, S.J. Bennison, and M.J. Readey, Crack Stability and Strength Variability in Alumina Ceramics with Rising Toughness-Curve Behavior, *Acta Mater.*, 2000, **48**(2), p 565–578

49. D.S. Horn and G.L. Messing, Anisotropic Grain Growth in TiO2-Doped Alumina, *Mater. Sci. Eng. A*, 1995, **195**, p 169–178

50. S. Hori, H. Kaji, M. Yoshimura, and S. Sōmiya, Deflection-Toughened Corundum-Rutile Composites, *MRS Proc.*, 1986, **78**, p 283

51. B.-K. Jang and T. Kishi, Fabrication and Microstructure of Al2O3 Matrix Composites by In-Situ Reaction in the Al2O3-La2O3 System, *J. Ceram. Soc. Jpn*, 1998, **106**(1236), p 739–743

52. J.B. Wachtman, W.R. Cannon, and M.J. Matthewson, Mechanical Properties of Polycrystalline Ceramics in General and Design Considerations. in *Mechanical Properties of Ceramics*, 1st edn. (Wiley, Hoboken, NJ, USA, 2009), pp 431–437

53. J.B. Wachtman, W.R. Cannon, and M.J. Matthewson, Effect of Microstructure on Toughness and Strength. in *Mechanical Properties of Ceramics* (Wiley, Hoboken, NJ, USA, 2009), pp. 199–225

54. R.W. Rice, Effects of Environment and Temperature on Ceramic Tensile Strength-Grain Size Relations, *J. Mater. Sci.*, 1997, **32**(12), p 3071–3087

55. J.B. Wachtman, W.R. Cannon, and M.J. Matthewson, Overview of Toughening Mechanisms in Ceramics, in *Mechanical Properties of Ceramics*, 1st edn, (Wiley, Hoboken, NJ, USA, 2009), pp. 189–197

56. T.S.RCh. Murthy, B. Basu, R. Balasubramaniam, A.K. Suri, C. Subramanian, and R.K. Fotedar, Processing and Properties of TiB2 with MoSi2 Sinter-Additive: A First Report, *J. Am. Ceram. Soc.*, 2006, **89**(1), p 131–138

57. T. V. Lin and P.D. Ownby, Densification and Fracture Toughness Enhancement of Pressureless Sintered Aluminum Oxide-Titanium Diboride Composites, in *Proceedings of the 16th Annual Conference on Composites and Advanced Ceramic Materials: Ceramic Engineering and Science Proceedings,* Vol. 13 (1994), pp. 132–139